energies

Article

Aerothermal Dynamic Characteristics of Array Micro Ribs in Channel Flow

Ke Zhao, Xueying Li * and Jing Ren

Department of Energy and Power Engineering, Tsinghua University, Beijing 100084, China; zhao-k18@mails.tsinghua.edu.cn (K.Z.); renj@tsinghua.edu.cn (J.R.)
* Correspondence: li_xy@tsinghua.edu.cn; Tel.: +86-186-1186-7685

Abstract: With the rising complexity of internal cooling structures in gas turbine blades, the limited cooling air volume and pressure head provided by the compressor have become significant constraints to further enhancements in the overall efficiency of gas turbines. To address this, micro-turbulators have been proposed as a viable solution in recent research. The rib turbulators, as a typical internal cooling structure, have inherent limitations in heat transfer measurements. In this study, a segmented lumped parameter method was employed to experimentally analyze the aerothermal dynamic characteristics of micro ribs under varying rib heights and Reynolds numbers in channel flow. It was found that heat transfer performance closely correlates with both rib height and the height of the incoming boundary layer. Under certain conditions of dimensionless height and dimensionless number, optimal heat transfer enhancement near the micro-rib was observed, leading to an approximately 30% increase in the overall thermal performance (OTP) compared to the results from research into traditional 90° ribs. Numerical results based on the Reynolds stress model (RSM) suggest that this improvement is primarily due to the increased turbulence intensity in the near-wall region (y^+ = 20–55) of the boundary layer caused by the micro ribs. This study presents a new characteristic parameter $e^+/\sqrt{Re}$ that offers improved representation of the heat transfer performance of micro ribs, and reveals that when this parameter is around 40, micro ribs can provide high heat transfer with low pressure loss, thereby improving the overall efficiency. These results underscore the potential applicability of micro ribs in advancing the efficiency of gas turbines and other related fields.

Keywords: gas turbine cooling; micro ribs; heat transfer; pressure loss; CFD; lumped parameter method; boundary layer

Citation: Zhao, K.; Li, X.; Ren, J. Aerothermal Dynamic Characteristics of Array Micro Ribs in Channel Flow. *Energies* **2023**, *16*, 5986. https://doi.org/10.3390/en16165986

Academic Editor: Andrea De Pascale

Received: 24 July 2023
Revised: 8 August 2023
Accepted: 12 August 2023
Published: 15 August 2023

1. Introduction

In pursuit of superior cycle thermal efficiency and the reduction in pollutant emissions, the inlet temperature of gas turbines has experienced a notable escalation. Consequently, turbine inlet temperatures often exceed the melting point of metal components. Due to limitations associated with air coolant, it is necessary to develop efficient and effective cooling technologies.

Internal cooling is a primary technique in turbine blade cooling, which often makes use of rib turbulators installed at periodic intervals in serpentine channels within the turbine blade. As cooling air flows through the ribs, the boundary layer separates and reattaches; secondary flows are also created in the channels, which improve mixing and heat transfer. The correlations between heat transfer and friction have been described by Webb [1]. The performance of heat transfer in a stationary ribbed channel is primarily determined by the channel aspect ratio (AR), rib shape, Reynolds number (*Re*), blocking ratio (e/D), spacing ratio (p/e), and rib angle (α) [2]. In the following decades, further research on ribs greatly expanded the range of research parameters for ribbed channels, and many engineering-related flow and heat transfer properties of ribbed channels have been experimentally and numerically summarized [3–16], as shown in Table 1. The blocking ratio (e/D) is one of the main factors affecting the heat transfer performance of the ribbed channel. In most studies, the blocking ratio ranges from 0.05 to 0.3.

Table 1. Research on rib cooling.

Reference	Rib Configurations	AR	e/Dh	p/e	*Re*	α
Han [3]	Transverse rib	1/4–4	0.047, 0.078	10, 20	10,000–60,000	90°
Tanda [4]	Transverse rib, Angled rib, V-ribs, Broken ribs	5	0.15,0.25	8, 13.3	9000–35,500	45°–90°
Liou [5]	Transverse rib	2	0.133	10	33,000	90°
Taslim [6]	Transverse, Angled, V-Shaped, Discrete Ribs	2	0.083–0.167	10	5000–30,000	45°, 90°
Park [7]	Angled rib	1/4–4	0.047, 0.078	10	10,000–60,000	30°–90°
SriHarsha [8]	Continuous ribs, V-broken ribs	1	0.0625–0.25	10	10,000–30,000	60°, 90°
Cho [9]	Transverse, Angled ribs		0.08	8		60°, 90°
Tanda [10]	Angled ribs	5	0.09–0.15	6.6–20	8900–36,000	45°
Wright [11]	Angled ribs	3	0.079	2.6–14.6	10,000–70,000	45°
Hossain [12]	Angled ribs		0.0264	15	100,000–200,000	45°, 90°
Dees [13]	Transverse ribs,				10,000–40,000	90°
Coletti [14]	Angled ribs,			7.5	67,500	30°
Liou [15]	Transverse rib	1.41	0.1	10	10,000	90°
Kaewchoothong [16]	Transverse rib, Angled rib, V-ribs, Broken ribs	2.5	0.18	10	400–1200	30°–90°
Present work	**Transverse ribs**	**4**	**0.0063–0.063**	**10–100**	**5000–60,000**	**90°**

Conventional internal cooling techniques are known to positively impact the heat transfer of turbine blade surfaces. Despite this, some scholars have noted that these methods predominantly find application below the Reynolds number line. This indicates that while flow losses increase, heat transfer enhancement remains limited. Drawbacks in large-scale cooling are significant, and a shift toward micro-cooling methods has therefore gained attention. Bunker thoroughly discussed this shift and its underlying reasons. Studies indicate that micro-cooling structures significantly decrease cooling airflow by up to 40%, while lowering thermal stress by 50% [17]. Considering the pressure loss constraints associated with turbine blades, there is a critical need to develop cooling techniques that operate above the Reynolds analogy line. Early insights into surface roughness and the recent advancements in active control of surface turbulators, inspired by bionics, suggest that micro-structures hold the potential to significantly enhance the heat transfer coefficient while minimizing flow losses to the maximum extent possible [18]. This has led to an increased research interest in surface micro ribs, a typical example of such surface structures.

The initial perspective on the application of micro-turbulators comes from research on surface roughness. The effect of roughness in fully turbulent boundary layers and channel flows has been addressed by several researchers, starting with the classic work of Nikuradse [18]. In TBL, Townsend's wall similarity hypothesis states that the turbulent motions outside the roughness sublayer are independent of the surface roughness. Jiménez [19] reviewed a variety of roughness topologies investigated by several researchers and noted that the dimensionless parameters, dimensionless height e^+ and blockage ratio δ/e, control the effect of roughness on turbulent boundary layers. According to Chung's review [20], the surface roughness in the transition region exhibits flow and heat transfer mechanisms that differ from those of fully rough behavior. For most micro-turbulators located in the transitional zone of the boundary layer, they exhibit complex behaviors that are similar to those of transitional surface roughness. Scholars began to pay attention to the combined effects of micro-turbulators on flow and heat transfer. Previous studies analyzed the flow and heat transfer characteristics of longitudinal vortex turbulence elements in the boundary layer [21–23] and channel flow [24–27]. The performance and layout of these longitudinal vortex turbulence elements were compared. The results show that the surface roughness can not only reduce the boundary layer and cause the macroscopic mixing of fluid, but also increase the turbulence intensity, which leads to better heat transfer. Mulhearn [28] investigated turbulent flow across a surface roughened by regularly spaced, two-dimensional roughness elements, and observed that the measured Reynolds shear stress decreases as the surface is approached. Savage et al. [29] investigated the effect of micro-turbulators on heat and momentum transfer. The increase in heat transfer coefficient is due to a change in the turbulence pattern close to the wall brought about by the presence of the surface protuberances. Furthermore, micro-turbulators are widely used in other cooling approaches, such as impinging jets. Gabour and Lienhard [30] measured stagnation region heat transfer coefficients, including beneath single hole impingement jets. Results show that stagnation region heat transfer coefficients increase by as much as 50 percent, relative to smooth surface values, which is attributed, in part, to the reduced boundary layer thickness associated with the impact and development of impingement flow along target plate surfaces. Ren et al. [31], both experimentally and numerically, examined the effect of rectangular and triangular surface roughness on the jet impingement cooling augmentation. Oda and Takeishi et al. [32] carried out experimental and numerical studies on heat transfer enhancement of single hole impingement cooling on a ribbed target surface. Currently, the majority of the research on micro-turbulators focuses on flow and heat transfer effects of different cooling forms or different shapes. However, the effect of the characteristic size of micro-turbulators on the flow and heat transfer, as well as its interaction with the boundary layer, has not been sufficiently investigated.

Furthermore, the surface heat transfer coefficient is a highly significant parameter. At present, the commonly employed internal cooling measurement methods include point measurement based primarily on a thermocouple, and surface measurement based mainly on liquid crystal or infrared imagery to determine temperature distribution. From the perspective of measurement principles, these methods are mainly divided into two categories: steady-state measurement and transient measurement. In addition to the previously mentioned approaches that are applied to the ribs, examples of this type of measurement method in internal cooling are now presented.

Hahn et al. [33] aimed to investigate the heat transfer rate in an internal passage of a typical gas turbine blade with various internal geometries, using multiple thermocouples placed on the surface of a heating plate and distributed along the channel. Four rib geometries, wrapped in copper foil, were then positioned on the heating plate. Benson et al. [34] experimentally studied the complex internal cooling flow in gas turbine blades using steady-state infrared (IR) thermometry. Based on quantitative and qualitative comparisons, flow velocity and cooling performance showed a strong correlation within the flow channel. The uncertainty in the measurement of the Nusselt number is approximately $\pm 10\%$. Choi et al. [35] studied the heat transfer and air-cooling problem of the trailing edge of a notched turbine blade and the effect of lateral impingement of two rows of passive elements on cooling gas using steady-state liquid crystal measurement technology. Cunha et al. [36] proposed closed-form analytical solutions for transient liquid crystal methods to describe the temperature distribution of four typical trailing edge configurations. Amro et al. [37] used a triangular channel with rounded edges as a model for the leading edge cooling channel of gas turbine blades and studied the heat transfer characteristics of internal cooling in circular-edged triangular channels in the Reynolds number range of 50,000–200,000, finding that the most efficient rib arrangement for leading edge cooling is a dual-sided overlap of 3D ribs at a 45-degree angle and a curved region. Funazaki et al. [38] used acrylic resin to manufacture two flow channel test models and evaluated the internal and external heat transfer coefficients and cooling efficiency of the test models using transient liquid crystal methods. Schüler et al. [39] aimed to analyze the influence of sidewall mass extraction on the pressure loss and heat transfer distribution in the two channels with cooling channels in the direction of the trailing edge flow. Saha et al. [40] conducted experimental studies on simulated turbine blade internal cooling channels, using inclined grooves and groove–rib combinations to enhance heat transfer from the wall. Tariq et al. [41] measured the flow and heat transfer characteristics of continuous ribs and perforated ribs with different exit angles, and the results showed that perforated ribs are helpful in improving the distribution of the downstream stagnation zone. Since the transient heat transfer measurement method is based on the assumption of a semi-infinite plate and has strict requirements for the one-dimensional heat conduction assumption of the measured surface, there are strong three-dimensional effects in the disturbed flow ribs and their surrounding regions, which do not satisfy the semi-infinite plate assumption and are bound to introduce errors into the measurement.

As observed, there are certain limitations to the measurement principles of common steady-state and transient heat transfer measurement methods. In the case of micro ribs, the rib itself and its surrounding areas exhibit strong three-dimensional effects compared to larger-scale ribs, making it challenging to accurately measure heat transfer. For example, in steady-state measurements using thermocouples, the heat transfer of the ribbed portion is often averaged in the final result. However, in liquid crystal measurements, due to the aforementioned difficulties with principles and measurement conditions, the heat transfer enhancement of the rib itself is often not considered. Therefore, to comprehensively evaluate the cooling effectiveness of micro ribs, an accurate and comparable experimental method needs to be developed.

In the present research, the aerothermal characteristics of micro-ribbed channels under array conditions were obtained by a PID-controlled segmented lumped parameter method, to evaluate the heat transfer performance in a channel with different rib heights and Reynolds numbers. The measured blocking ratios (e/D) ranged from 0.0063 to 0.063. The Reynolds number ranged from 5000 to 60,000. Based on the boundary layer parameters of the incoming flow, the dimensionless height ($^{e+}$) of all operating conditions was set between 2.8 and 281. The numerical results obtained from the Reynolds stress model (RSM) were used to analyze the experimental results.

2. Experimental Setup and Procedure

Specific details of measurement and parameter determinations are presented for the experimental facility at Tsinghua University in Beijing, China, and shown in this section.

2.1. Experimental Apparatus

Figure 1a presents the facility used for the experiment, including the test section, PID controller, data acquisition, pressure transducer, mass flowmeter, plenum and the test section. A centrifugal flowmeter is installed behind the measuring section to measure the mass flow. The suction wind tunnel is realized by the suction generated by the blower, ensuring that the incoming flow temperature is not affected by the temperature rise of the blower.

Figure 1c shows the arrangement of the test section. The flow channel of the test section is designed to minimize heat loss and air leakage. The test section consists of eight copper blocks, each measuring 20.0 mm wide, 80.0 mm long, and 12.0 mm thick. Insulating materials are installed between adjacent copper blocks. In this arrangement, copper blocks serve as regional heat transfer surfaces to maintain a uniform temperature. Three machined holes are used on the centerline of each copper block to accommodate three different installation depths of thermocouples. Thermal films were applied to the bottom of each copper block to provide a constant surface heat flux boundary condition. On the side of the thermal film facing the environment, insulation foam was injected using a glue gun to create an insulation layer, minimizing heat losses and providing additional mechanical support to the copper blocks. In this study, the thermal film provided a surface heat flux density ranging from 0 to 5 kW/m^2. The temperature range of the copper blocks is from 30 °C to 80 °C. Small holes with a diameter of 1 mm were arranged before and after the test section, and two micro-pressure transmitters with a range of ±12.45 Pa and ±245 Pa were used to measure the average static pressure through the micro-rib front and rear passages, to meet the precision requirements of different pressure ranges under different work conditions.

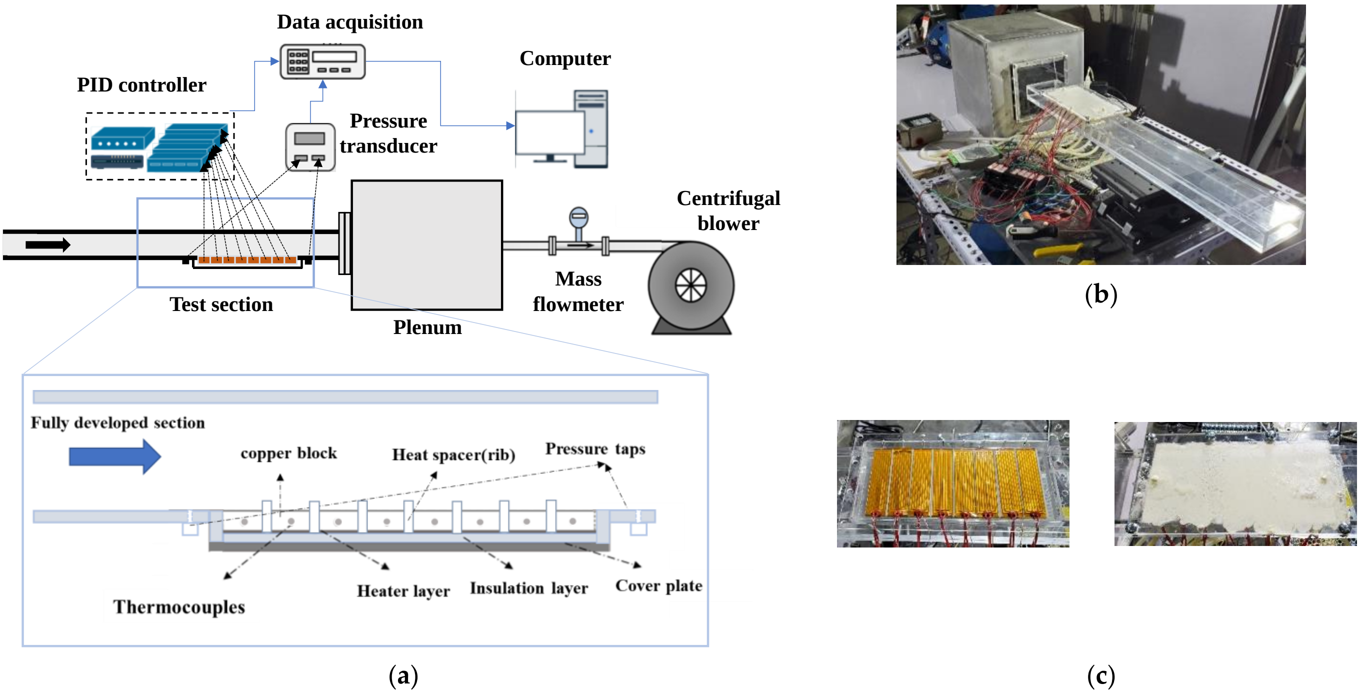

Figure 1. Experiment facility: (**a**) schematic of the experiment facility; (**b**) fully developed section and test section; (**c**) copper blocks with film heater and insulation layer.

The test section consists of a copper block, an insulation sheet, a heating film, and an insulation layer. The insulation sheets between the copper blocks are made of processed ABS plastic and processed to a suitable height, serving as the ribs for the study. The purpose of this approach is to eliminate the influence of the rib's own heat transfer. The copper block and the insulation sheet are installed sequentially on one side of the runner, and a caulking agent with low thermal conductivity (0.022 W/(m·K)) is injected on the outer side as an insulation layer. Since the thermal conductivity of the copper block (401 W/(m·K)) is much larger than that of the insulation sheet (0.25 W/(m·K)), each copper block separated by the insulation sheet satisfies the measurement conditions of the lumped parameter method. That is, it can be assumed that the internal temperature of each copper block can be stabilized at the same temperature in the steady state.

2.2. Experiment Design

The flow and heat transfer performance of micro-rib heights were investigated by machining ribs of different heights on a copper block, as shown in Table 2. The width and height of the ribs are consistent with the width and height of the channel, to ensure they can be placed tightly in the channel from the outside. Ribs of different heights, ranging from 0.2 mm to 2 mm, were machined on the inner side of the channel, with e/D ranging from 0.0063 to 0.0625 and maintaining a width-to-height ratio (W/H) of 4. The flow and heat transfer characteristics were measured under different working conditions with Reynolds numbers ranging from 5000 to 60,000. The total length of the channel is 1000 mm, with the ribbed section placed at 700 mm to ensure fully developed flow.

Table 2. Experiment parameters.

L (mm)	1000
L_s (mm)	700
W (mm)	80
H (mm)	20
e (mm)	0.2, 0.4, 0.6, 1, 2
p (mm)	10
D (mm)	32
e/D	0.0063, 0.0125, 0.0188, 0.0313, 0.0625
W/H	4
Re_{in}	5000, 10,000, 20,000, 40,000, 60,000

As the micro ribs are all merged in the turbulent boundary layer, the dimensionless height of the micro ribs is determined by the boundary layer's dimensionless scale:

$$e^+ = \frac{u_\tau e}{\nu} \tag{1}$$

where u_τ is the friction velocity of incoming flow.

For the experiment, e^+ can be determined by the measured friction factor and Reynolds number:

$$e^+ = (\frac{f}{2})^{1/2} Re \frac{e}{D} \tag{2}$$

In this study, according to different values of the Reynolds number, the value of e^+ varies between 2.794 and 280.9. In order to investigate whether the value of e^+ has a significant impact on the effect of micro ribs, RANS numerical simulation was added to the condition of the gray part in Table 3 to analyze the effect of flow parameters on the characteristics of micro ribs.

Table 3. Experimental and numerical cases.

e^+	0.2 mm	0.4 mm	0.6 mm	1 mm	2 mm
5000	2.794	5.588	8.382	13.97	27.94
10,000	5.16	10.32	15.48	25.8	51.6
20,000	10.43	20.86	31.29	52.15	104.3
40,000	18.282	36.564	54.846	91.41	182.82
60,000	28.09	56.18	84.27	140.45	280.9

2.3. Heat Transfer Measurment Techniques

The lumped parameter method was used to measure the heat transfer coefficient, and the typical heat transfer diagram of the copper block is shown in Figure 2. The thermal conductivity of the copper block is 401 W/m·K. To evaluate the uniformity of temperature inside the copper block, the Bi number is introduced as follows:

$$Bi = \frac{l \cdot h}{k} \tag{3}$$

where l is the characteristic length, generally taken as the ratio of the body volume to the heat transfer area; and h and k are the convective heat transfer coefficient and the thermal conductivity of the object surface, respectively. In the experiment, the Bi number of the copper block is significantly less than 0.1, indicating that the temperature distribution inside the copper block is uniform and satisfies the condition of the lumped parameter method.

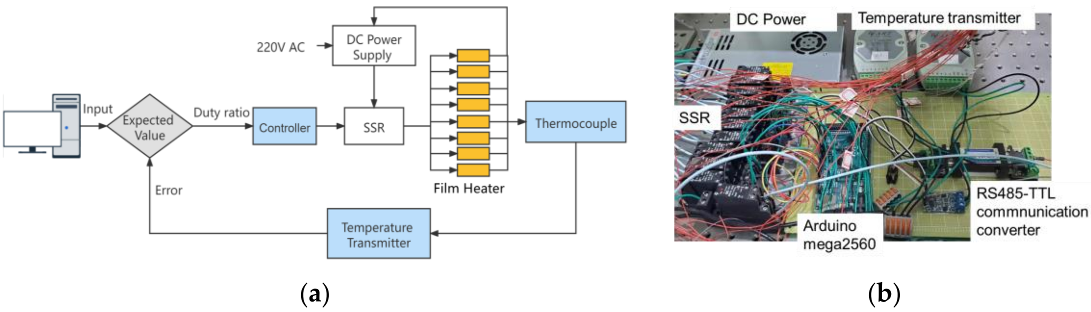

Figure 2. PID controller: (**a**) schematic of PID controller; (**b**) PID controller system.

Since the copper block meets the central parameter conditions, the final heat transfer coefficient with the projection area as the heat transfer area is obtained as follows:

$$h_{au} = \frac{q}{(T_w - T_f)} \quad (4)$$

where T_w and T_f represent the temperature of the copper block and the stagnation temperature of the supply gas chamber, respectively, and q is the heat flux density. h_{au} represents the heat transfer coefficient with the projected area

The steady-state heat flux density q is provided by the heating film attached to the back of the copper block. The heat flux density is determined by measuring the resistance and voltage of the heating film as follows:

$$h_f = \frac{q - \frac{\lambda}{b}(T_w - T_f) - \sigma(T_\infty^4 - T_w^4)}{T_w - T_f} = \frac{q - q_{loss}}{T_w - T_f} = \frac{U^2 - U_s^2}{RA(T_w - T_f)} \quad (5)$$

where A is the area of the lower surface of the copper block, which is the same as the projected area of the upper surface of the copper block. U and R are the voltage and resistance of the heating film, respectively, and are measured by a digital multimeter. The heat loss q_{loss} is calculated using finite element analysis and one-dimensional heat conduction analysis. The specific analysis process is described in Section 2.4.

In the present experiment, the heat flow output is controlled by a PID system to ensure the same temperature for each copper block. The average heat transfer coefficient at the location of each copper block is calculated with the obtained heat flux. The heat loss in the steady-state measurement is quantified by measuring the heat flow density at the same copper block temperature at rest. The schematic of the PID controller system is shown in Figure 2.

The PID temperature control system and heat flux density measurement system have two functions and goals: 1. To ensure that the temperature of the copper block quickly, stably, and accurately reaches the given value under different flow conditions. 2. To measure the heat flux density that maintains the temperature of a certain copper block with high accuracy, which can be used to quantify experimental errors.

The heat loss can be measured during the experiment due to the use of the PID temperature control system and the heat flux density measurement system. The specific evaluation method is as follows: conducting a preliminary experiment without the main flow, setting the target temperature of the copper block T_c, and automatically adjusting it using the PID to make the temperature reach the target value. The measured heat flux density at this temperature is the heat loss q_{loss} at this temperature. Based on this, the formal experiment is carried out with the main flow applied, and the temperature of the copper block decreases. The PID system adjusts the heat flux density automatically to return the temperature of the copper block to the target value Tc. At this time, the measured heat flux density minus the heat loss obtained from the preliminary experiment represents the net heat flux density at this temperature and flow condition. By evaluating heat dissipation in this way, all known and unknown heat dissipation losses can be evaluated accurately and reliably.

2.4. Uncertainty Analysis

This section focuses on the main parameters that affect the uncertainty of heat transfer measurement, including environment temperature, copper block temperature, voltage, and resistance. The temperature uncertainty in the environment is estimated to be about 0.1 K. Temperature uncertainty in copper bars is estimated to be about 0.5 K, which is a combination of the thermocouple temperature (0.1 K) and the heat conduction within the copper block (0.4 K). The experimental uncertainties of voltage and heater resistance measurements are 0.144 V and 0.1%, respectively. The uncertainty quantification of Equation (5) is applied, as shown in Equation (6). Because the machining accuracy of the copper block size is 0.01–0.015 mm, the uncertainty of the area A of the copper block is a higher-order small quantity, which is omitted in the calculation. The uncertainty of the experiment is calculated by other uncertainties. An uncertainty analysis is conducted for a typical case with e/D = 0.063 and Re = 20,000. As shown in Table 4, the maximum uncertainty for the heat transfer coefficient is about 7%. Based on the measuring range of the micro-pressure gauge and the pressure drop range of the experimental conditions, the uncertainty of the pressure drop and the resistance coefficient in this experiment are 3.5% and 5%, respectively. The uncertainty quantification method in this study is based on Moffat's approach [42].

$$\delta h_f = \sqrt{\left(\frac{\partial h_f}{\partial U}\delta U\right)^2 + \left(\frac{\partial h_f}{\partial U_s}\delta U_s\right)^2 + \left(\frac{\partial h_f}{\partial R}\delta R\right)^2 + \left(\frac{\partial h_f}{\partial A}\delta A\right)^2 + \left(\frac{\partial h_f}{\partial T_w}\delta T_w\right)^2 + \left(\frac{\partial h_f}{\partial T_f}\delta T_f\right)^2} \tag{6}$$

Table 4. Uncertainty analysis.

Quantity	Values	Error	ecr (%)	Copper Bar Number	Uncertainty
h (W/(m^2·K))	103.34	-	-	1	5.60%
U (V)	11.13	0.144	2.58	2	6.31%
R (Ω)	28.8	0.1	0.35	3	6.14%
q_{loss} (W/m^2)	83.7	7.17	0.27	4	7.12%
T_w (°C)	50	0.5	2.0	5	6.74%
T_f (°C)	25.1	0.1	0.4	6	7.08%
Uncertainty (%)	-	-	5.60	7	6.76%
				8	7.13%

The heat insulation sheet is machined and integrated to ensure the same rib height at different positions of the same group of cases through integrated processing, and the uncertainty of ABS material processed using the machine tool is less than 0.01 mm.

3. Numerical Methodology and Data Reduction

3.1. Numerical Setup

The numerical simulations were performed with the CFD software FLUENT 19.0. The Reynolds stress model (RSM) is adopted in this research. RSM solves the Reynolds stress transport equation as well as the dissipation rate equation directly instead of using the vortex viscosity assumption to close the equations. Therefore, it requires solving seven additional equations in the three-dimensional solution. Compared with the traditional RANS vortex viscosity model, RSM has higher confidence in its separation flow prediction. The Reynolds stress model has a natural theoretical advantage for flow phenomena with Reynolds stress anisotropy, such as reverse pressure gradient and surge-induced separation, because the Reynolds stress and its component relationships are not modeled. The channel used for CFD is consistent with the geometry of the experiment, and its parameters are shown in Table 2. The relevant boundary conditions are shown in Figure 3. The detailed information for the numerical methods and boundary settings is shown in Table 5, and the mesh condition is shown in Figure 4.

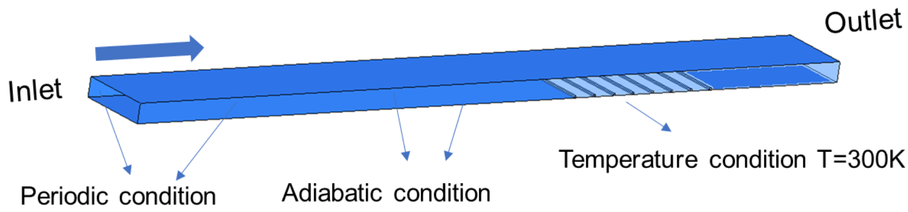

Figure 3. Model geometry and boundary settings.

Table 5. Numerical methods and boundary settings.

NUMERICAL SETTINGS	
TURBULENCE MODEL	Reynolds stress model with enhanced wall treatment, linear pressure
MESH SETUP	Structure mesh, near-wall $\Delta y^+ = 1$ Grid number is about 3.9 million
BOUNDARY CONDITION	
INLET	Mass flow inlet, T = 320 K
OUTLET	Pressure outlet, gauge pressure = 0
SIDE SURFACE	Periodical boundary condition
SURFACE BETWEEN THE RIBS	No slip stationary wall, temperature thermal condition T = 300 K
RIB SURFACE AND OTHER SURFACE	Adiabatic condition

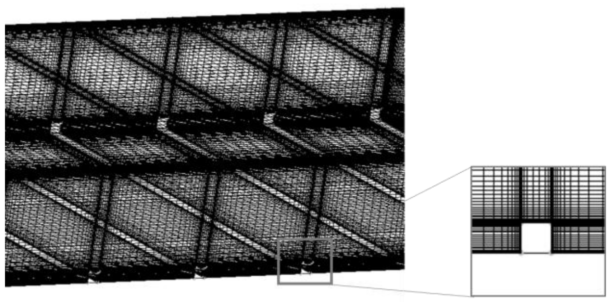

Figure 4. Grid representation.

3.2. Data Reduction

To analyze the numerical results, the following definitions are provided:

$$Re = \frac{u_m D}{v} \tag{7}$$

where u_m represents the bulk velocity, D represents the hydraulic diameter of the channel. v represents fluid kinematic viscosity. For the CFD case, temperature boundary conditions are implemented for all channel walls except rib surfaces. The heat transfer coefficient is given by the equation:

$$h = \frac{q_w}{(T_m - T_w)} \tag{8}$$

The channel's heat transfer is nondimensionalized through the Nusselt number, and the definition of spatially averaged Nusselt number is as follows:

$$\overline{\overline{Nu}} = \frac{\iint_s NudS}{S} = \frac{\iint_S hdS}{S} \times \frac{d}{\lambda} \tag{9}$$

In order to eliminate the effects of inlet and outlet disturbances, the area for S is chosen to be the region between the 4th and 7th copper blocks, consistent with the experimental setup.

Using the pressure difference between the calculated areas, the fanning friction factor is used to calculate pressure losses in the channel, as follows:

$$f = \frac{\Delta P D}{2\rho {u_m}^2 L} \tag{10}$$

Heat transfer enhancement is evaluated by comparing the experimental Nusselt numbers with those for fully developed turbulent flow in a smooth channel. Fully developed turbulent flow Nusselt numbers in a smooth channel are calculated based on the Dittus–Boelter correlation. Friction factors for fully developed turbulent flow in a smooth channel are standardized using the Blasius correlation, as follows:

$$\begin{aligned} Nu_0 &= 0.023 Re^{0.8} Pr^{0.4} \\ f_0 &= 0.079 Re^{-0.25} \end{aligned} \tag{11}$$

Based on the flow and heat transfer characteristics of the channel, the overall thermal performance (OTP) of the channel was calculated, which is discussed and recommended according to Ref. [43]:

$$OTP = \frac{\overline{\overline{Nu}}/Nu_0}{(f/f_0)^{1/3}} \tag{12}$$

3.3. Numerical Validation

In all RANS simulations, the near-wall mesh was appropriately set to ensure that wall y^+ values were less than 1. A typical case with e/D = 0.0188 and Re = 20,000 was selected for grid independence validation. Four cases with different grid sizes were considered: 0.9 million, 1.8 million, 3.9 million, and 7.6 million elements as shown in Figure 5. The comparison of the average Nusselt number for cases 3 and 4 revealed that the difference between the finest and medium grid was less than 0.2%. Therefore, it was concluded that a grid size of 3.9 million elements balanced both economy and accuracy of computation, and was thus chosen for all calculations.

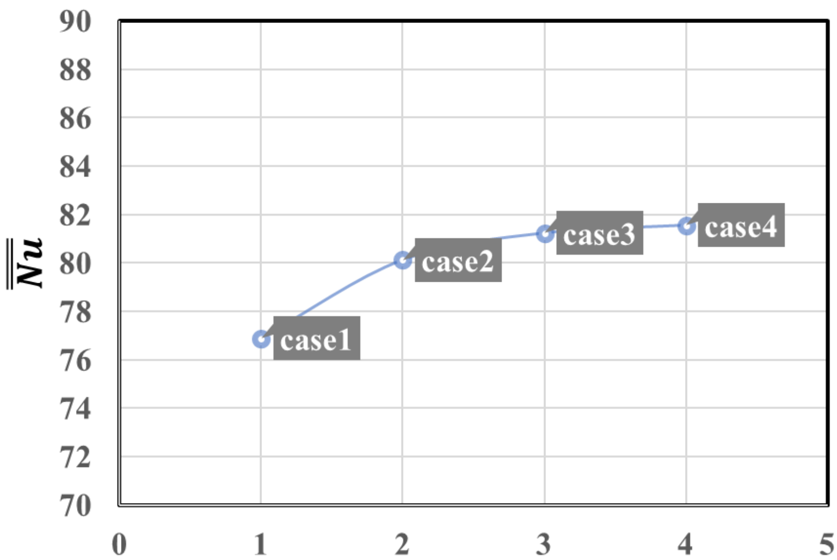

Figure 5. Grid independence test.

Figure 6 presents the trend of the average Nusselt number with respect to rib height, comparing numerical results from different turbulence models and experimental results.

Both the k-ε and k-ω models significantly deviate from the experimentally obtained trend to varying degrees. For instance, the k-ε model overall overestimates Nu at low rib heights, while the k-ω, SST, and Transition SST models underestimate the average heat transfer at high rib heights. Overall, although there are still quantitative differences, the RSM model qualitatively captures the trend of heat transfer performance observed in the experiments. Therefore, the RSM model was chosen for the analysis of flow field and turbulence information.

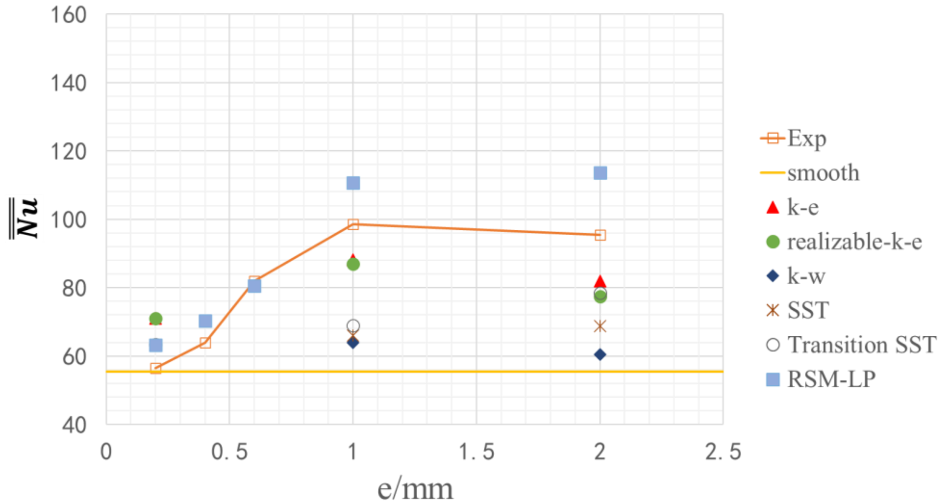

Figure 6. Comparison of different turbulence models.

4. Results and Discussion

First, before conducting all the experiments, a smooth channel experiment was conducted as a control, comparing it with the classical empirical correlation to validate the reliability of the experimental method. In Figures 7 and 8, the variations in pressure drop and average Nusselt number with Reynolds number ranging from 5000 to 60,000 are presented, and compared with the classical Blasius solution and Dittus–Boelter correlation, respectively. The experimental results are in good agreement with the correlation results, confirming the reliability of the experimental method.

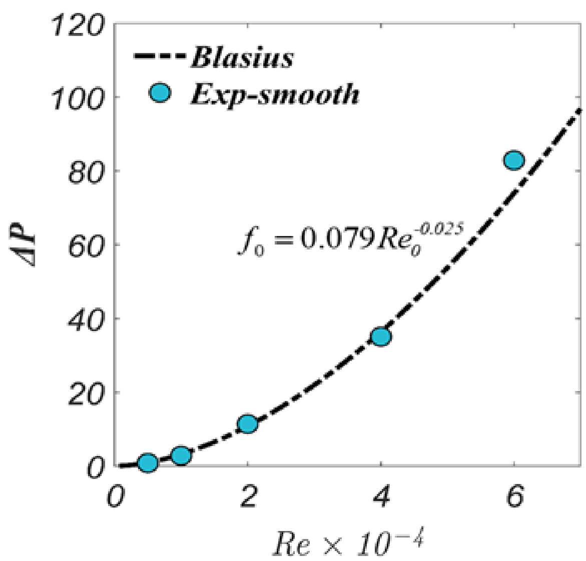

Figure 7. Experimental and numerical comparison of smooth channel pressure drop.

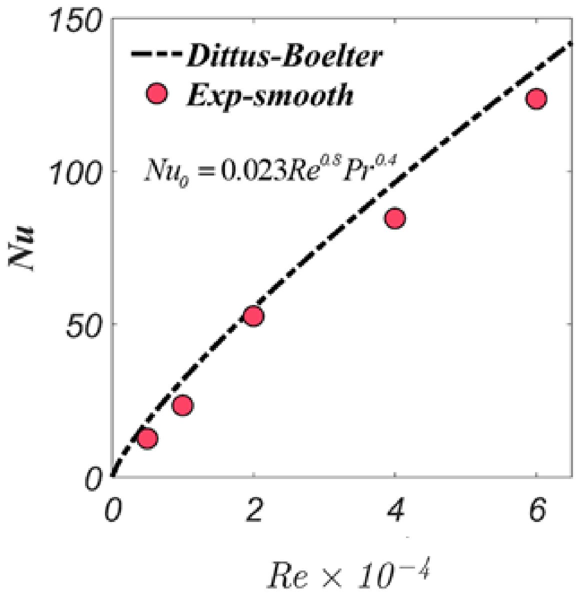

Figure 8. Experimental and numerical comparison of smooth channel Nusselt number.

4.1. The Resistance and Heat Transfer Characteristics of Arrayed Micro Ribs

This section mainly introduces the resistance and heat transfer characteristics of the array micro ribs obtained from experiments, analyzing and explaining them from two dimensions of experimental design: Reynolds number and rib height variations. Figures 9 and 10, respectively, show the trends of the resistance coefficient ratio and the Nusselt number under different e/D values. For the resistance coefficient, it keeps increasing with the increase in rib height, and the trends are roughly the same for different Reynolds numbers, except for slight differences at lower Reynolds numbers. This indicates that under high Reynolds numbers, the resistance coefficient amplification of each micro-rib height is similar, representing a strong correlation between the resistance coefficient amplification of the array micro ribs and rib height, and a relatively small relationship with Reynolds number variations. Regarding the Nusselt number, the trend is quite different from that of the resistance coefficient. At low Reynolds numbers, the Nusselt number continuously increases with increasing rib height. However, as the Reynolds number increases, the Nusselt number no longer increases with increasing rib height. When the Reynolds number reaches 40,000–60,000, the Nusselt number increases first and then decreases with increasing rib height.

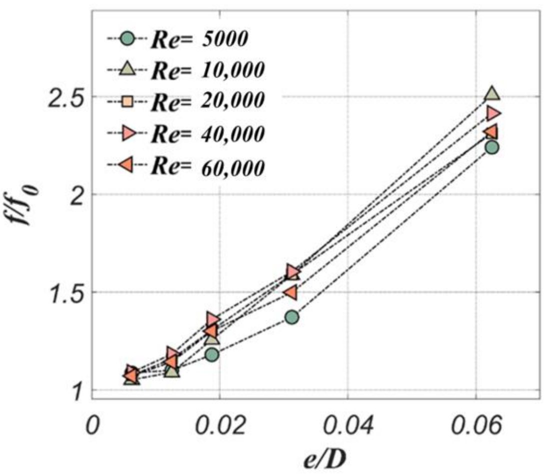

Figure 9. Friction factor ratio variation with *e/D*, for different *Re*.

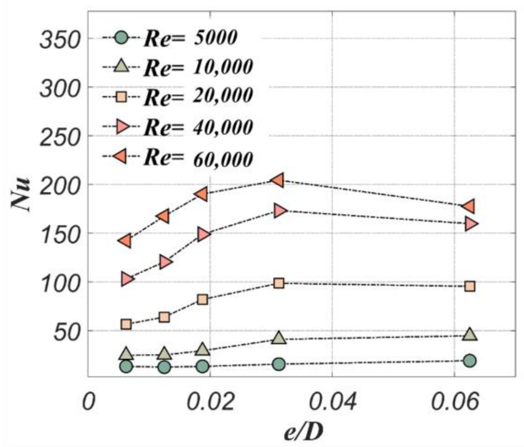

Figure 10. Nusselt number variation with *e/D*, for different *Re*.

Figures 11 and 12 show the trends of the resistance coefficient ratio and the Nusselt number ratio under different *Re* (Reynolds number) values. For the resistance coefficient, Figure 11 clearly demonstrates the fluctuation in the resistance coefficient amplification at low Reynolds numbers, while at high Reynolds numbers, the amplification remains almost unchanged with the variation in Reynolds number. Regarding the Nusselt number, it can be observed that, at different rib heights, the amplification of the Nusselt number increases first and then decreases with increasing Reynolds number, but the position of the inflection point varies with different rib heights.

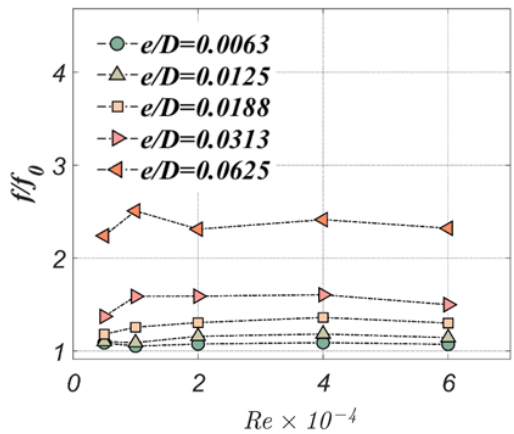

Figure 11. Friction factor ratio variation with *Re*, for different *e/D*.

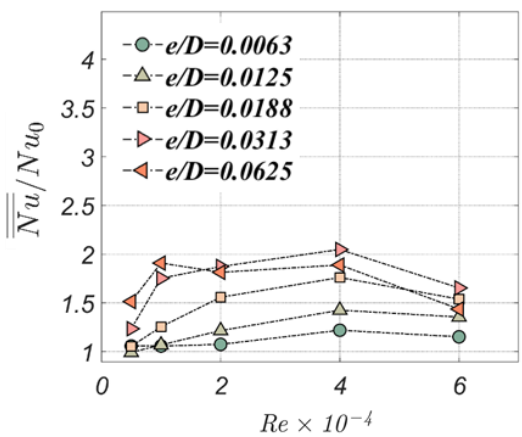

Figure 12. Nusselt number ratio variation with *Re*, for different *e/D*.

By observing the amplification of the resistance coefficient, it can be noted that when $Re > 20{,}000$, the amplification of the resistance coefficient tends to approach a constant value with increasing rib height. This indicates that at high Reynolds numbers, the micro-rib wall behavior is closer to that of a fully rough surface, and the amplification of the resistance coefficient is mainly influenced by the variation in rib height. On the other hand, the variation in the resistance coefficient at low Reynolds numbers is more chaotic, showing different amplification trends at different rib heights. Regarding the Nusselt number, it can be observed that both Reynolds number and rib height have significant impacts on its amplification. This leads to different dominant performances of the Nusselt number at different rib heights and Reynolds numbers. For example, at $Re = 20{,}000$, the working conditions with $e/D = 0.188$ and 0.313 exhibit optimal heat transfer performance ratios. A reasonable conjecture is that the influence of micro ribs on heat transfer performance is related to rib height and the height of the turbulent boundary layer, which will be further discussed in the following sections.

4.2. The Near-Wall Reinforcement Mechanism of Micro Ribs

Figures 13 and 14 show the comparison between experimental and numerical calculations of the drag coefficient and Nusselt number. Overall, the difference is relatively small; the maximum error between experimental and numerical results is less than 20%, as shown in Table 6, and the numerical calculations successfully capture the changes exhibited by the experimental data. Given the inherent computational bias in RANS calculations, it is believed that the RANS method used in this paper is effective in capturing the patterns expressed by the experimental data. Subsequently, the flow field data obtained from RANS calculations will be used for analysis in the following sections.

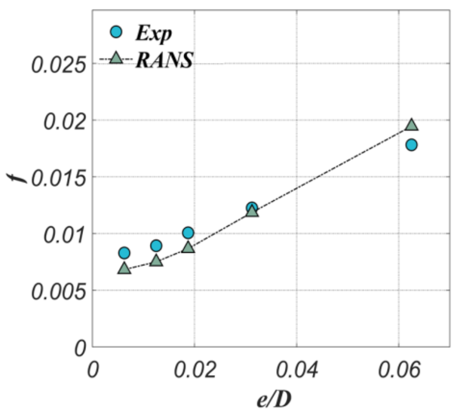

Figure 13. Experimental and numerical comparison of friction factor.

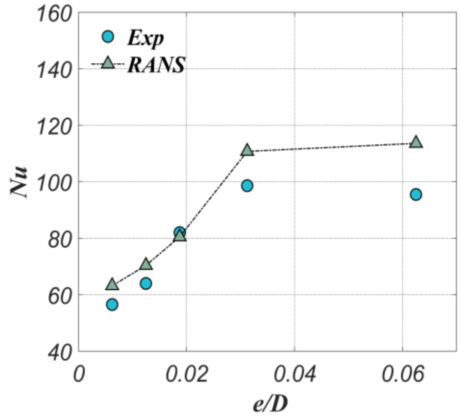

Figure 14. Experimental and numerical comparison of Nusselt number.

Table 6. The difference in friction factor and Nusselt number for the experiment and CFD.

Difference	*e*/*D* = 0.0063	*e*/*D* = 0.0125	*e*/*D* = 0.0183	*e*/*D* = 0.0313	*e*/*D* = 0.063
f	17%	16%	16%	7%	1%
Nu	12%	10%	2%	12%	19%

Figure 15 displays the relationship between streamline patterns and the corresponding shear stress on the wall between the ribs at different rib heights. It can be observed that as the rib height increases, the magnitude of shear stress on the intercostal wall initially increases and then decreases. The maximum magnitude is obtained when e/D = 0.0183, and overall, there is a strengthening trend in the region between the ribs. At this point, the main factor contributing to the increase in resistance is frictional resistance on the wall. However, when the rib height further increases, the shear stress on the wall decreases, and the recirculation zone between the ribs increases significantly. In the case of large rib heights, the resistance coefficient is mainly generated by the pressure difference caused by the ribs.

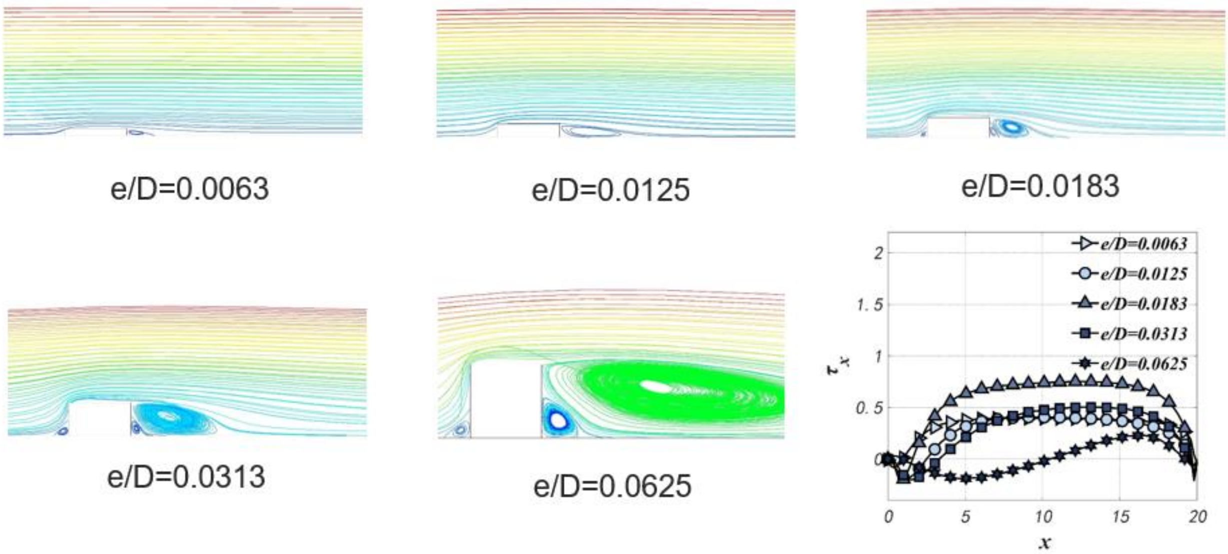

Figure 15. The streamline diagram near the micro ribs and the distribution of shear stress between the ribs for different e/D, for Re = 20,000.

Figure 16 explains the reasons for micro-rib resistance at different Reynolds numbers. At low Reynolds numbers (Re < 20,000), due to the thicker incoming boundary layer and the development of recirculation vortices, the morphology and extent of the recirculation zone exhibit unstable changes. This leads to variations in the resistance coefficient ratio with Reynolds number at lower Reynolds numbers. However, when Re > 20,000, the size and impact range of the recirculation vortices become relatively stable. Therefore, the resistance coefficient ratio does not vary with changes in the Reynolds number.

Figures 17 and 18 explain the mechanism of heat transfer enhancement in micro ribs by considering the variations in rib height and Reynolds number, respectively. By comparing the distribution of the average Nusselt number between ribs in Figure 15a and the distribution of turbulent kinetic energy at different y^+ values on the right side, it can be observed that the enhancement of turbulence intensity in the transition layer to the logarithmic layer (y^+ = 20–55) of the boundary layer is the main reason for heat transfer enhancement. Figure 16 further validates this point by considering different Reynolds numbers. It indicates that when the height of the ribs varies within the range of the non-dimensional height of this boundary layer, it can enhance the turbulence intensity in the near-wall region, thereby causing heat transfer enhancement. However, as the non-dimensional height further increases, the heat transfer in the near-wall region cannot be further enhanced, resulting in the inability to further improve the heat transfer capacity. Clearly, for heat transfer, both rib height and Reynolds number influences the heat transfer enhancement effect of micro ribs. This also suggests the use of non-dimensional rib height as a measure to assess the heat transfer performance of micro ribs. This viewpoint will be discussed in detail in the next section.

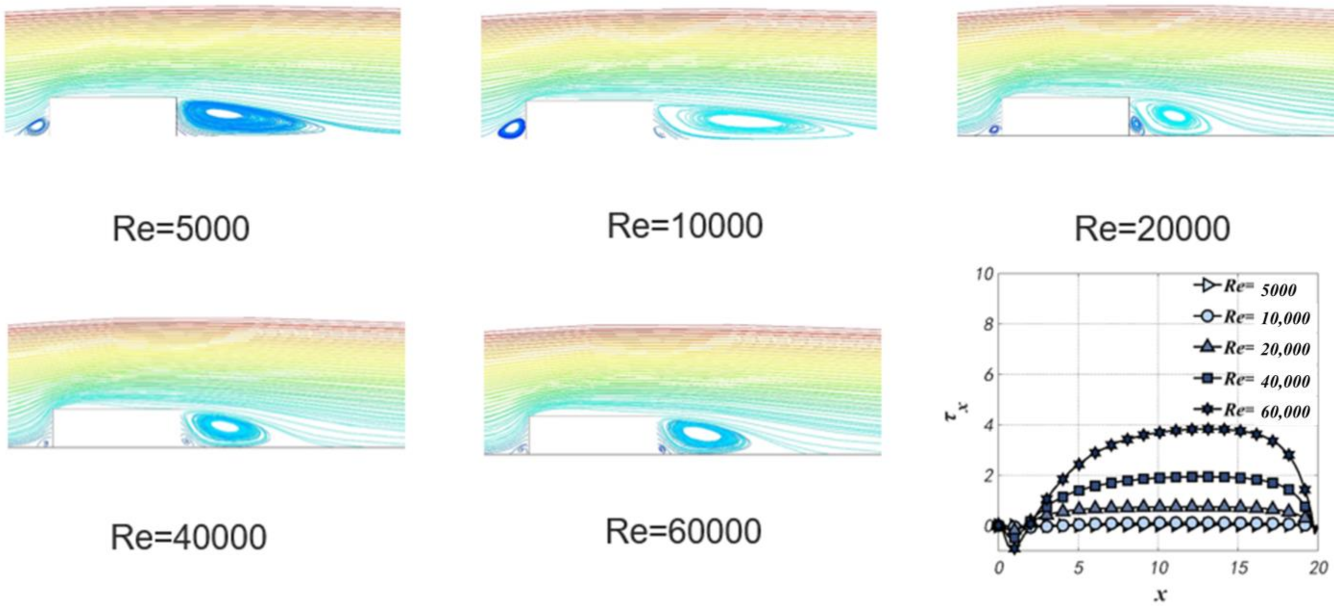

Figure 16. The streamline diagram near the micro ribs and the distribution of shear stress between the ribs for different *Re*, for e/D = 0.0183.

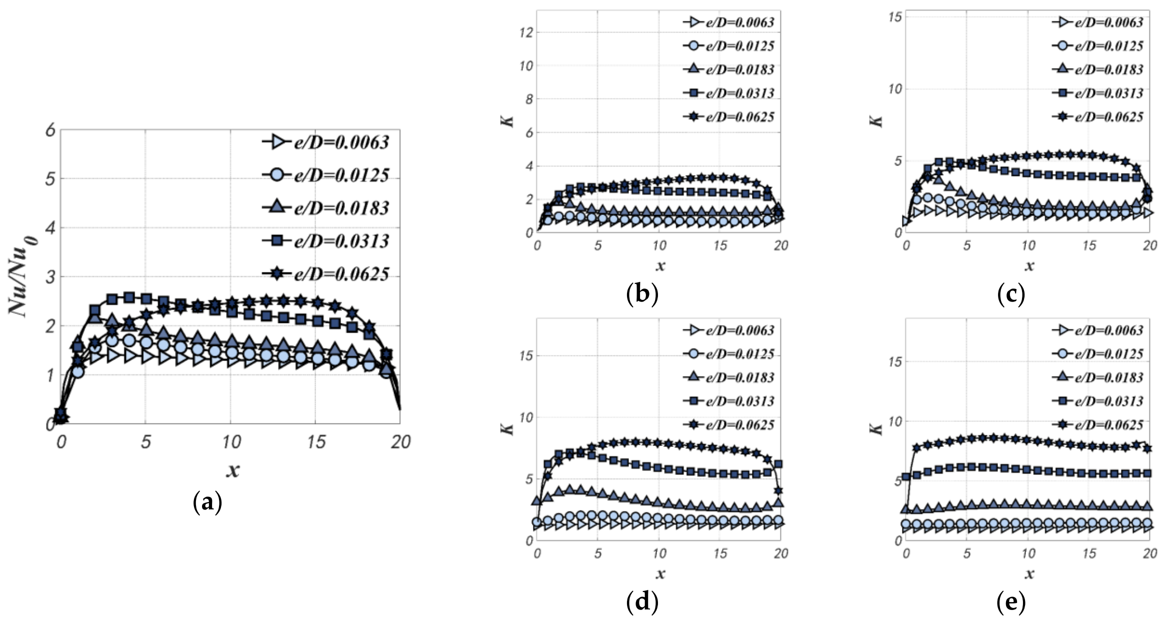

Figure 17. The distribution of the Nusselt number between the ribs for different e/D compared with turbulent kinetic energy at different y^+, for *Re* = 20,000: (**a**) spanwise averaged Nusselt number; (**b**) turbulence kinetic energy at y^+ = 10.86; (**c**) turbulence kinetic energy at y^+ = 21.72; (**d**) turbulence kinetic energy at y^+ = 54.29; (**e**) turbulence kinetic energy at y^+=108.58.

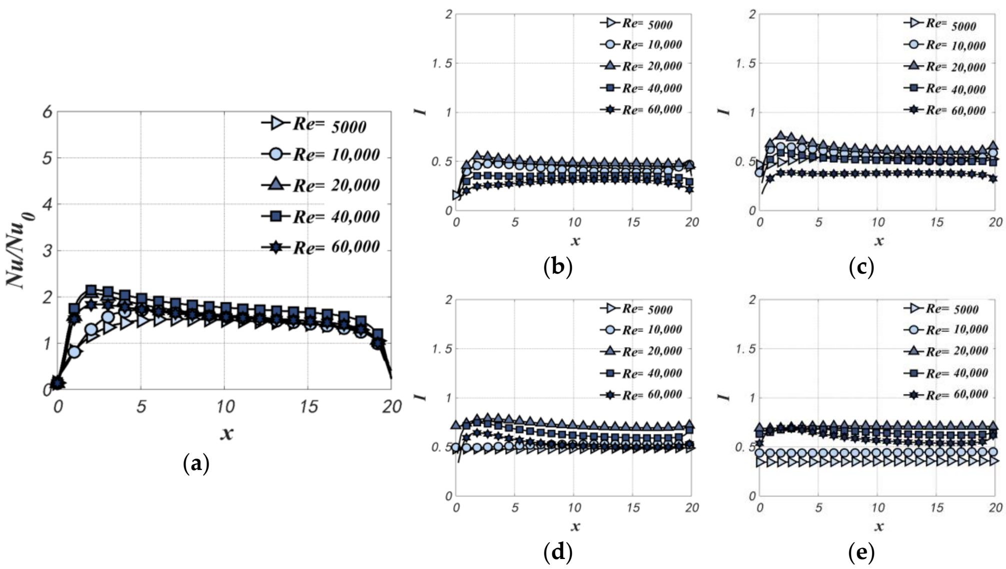

Figure 18. The distribution of the Nusselt number between the ribs for different *Re* compared with turbulent kinetic energy at different y^+, for e/D = 0.0183: (**a**) spanwise averaged Nusselt number; (**b**) turbulence intensity at y^+ = 10.86; (**c**) turbulence intensity at y^+ = 21.72; (**d**) turbulence intensity at y^+ = 54.29; (**e**) turbulence intensity at y^+ = 108.58.

4.3. Characteristic Dimensionless Numbers for Heat Transfer Enhancement of Micro Ribs

Regarding the experimentally obtained data on the resistance and heat transfer characteristics of the array micro ribs, this study employs the classical power-law form to fit the flow and heat transfer characteristics of the micro ribs. The fitting results are as follows:

$$\begin{gathered} Nu = 0.03537(e/D)^{0.1459}Re^{0.8289} \\ f = 1.765\left[(e/D)^{1.421} + 0.0148\right]Re^{-0.14} \end{gathered} \quad (13)$$

The coefficient of determination (R^2) for the fitting is 0.987 for the resistance coefficient and 0.975 for the heat transfer coefficient. For the resistance coefficient, as *e/D* approaches zero, there still exists a smooth channel resistance component based on frictional resistance. Therefore, a constant term has been added to the equation on *e/D*. Regarding the fitting results, the power-law exponents of *e/D* and *Re* provide a visual understanding of the relative influences of these two parameters on Nu and f. For example, for Nu, the influence of rib height is significantly smaller compared to the impact of Reynolds number, while for f, it is the opposite, with rib height dominating its effect. This can be visually observed from the fitting surfaces in Figures 19 and 20.

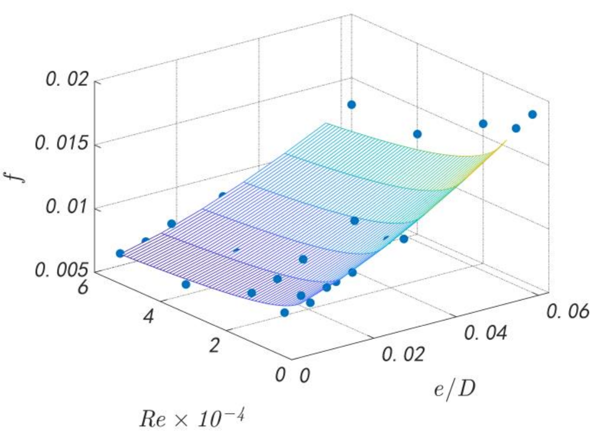

Figure 19. The fitting surface of the drag coefficient.

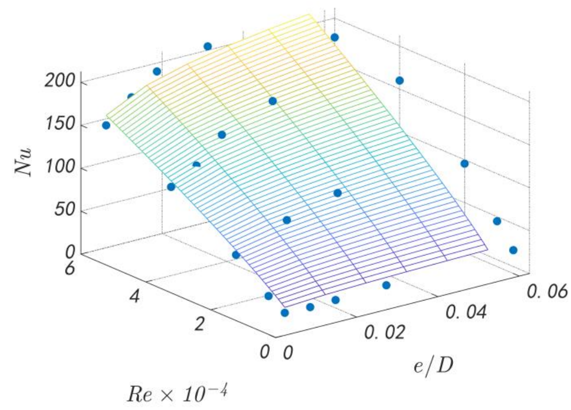

Figure 20. The fitting surface of the Nusselt number.

Figures 21 and 22 illustrate the comparison between the predicted and actual values of the drag coefficient and Nusselt number based on the correlation equations. It can be observed that although both overall trends are good, there are still certain deviations. As mentioned earlier, for the Nusselt number, a phenomenon of decreasing values can be observed for high Reynolds numbers and high e/D conditions, which is difficult to demonstrate in the form of power-law fitting. Therefore, this study uses the non-dimensional height of rib e^+ to redraw the experimental data. The results are shown in Figure 23, revealing that the Nusselt number, when solely using the non-dimensional height e^+, exhibits a good agreement trend at different Reynolds numbers. However, there is a deviation at low Reynolds numbers, which may be attributed to the incomplete turbulence behavior that may exist at low Reynolds numbers. The physical laws governing such behavior differ from those of fully developed turbulent boundary layers.

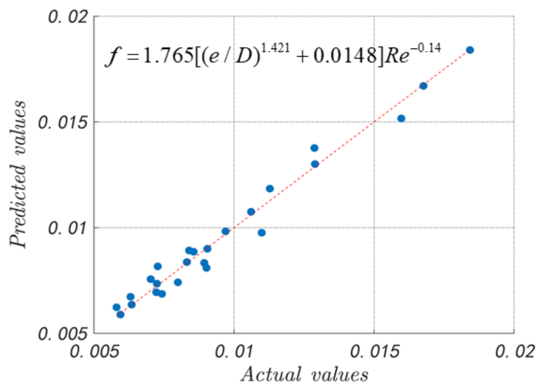

Figure 21. Predicted values vs. actual values for drag coefficient.

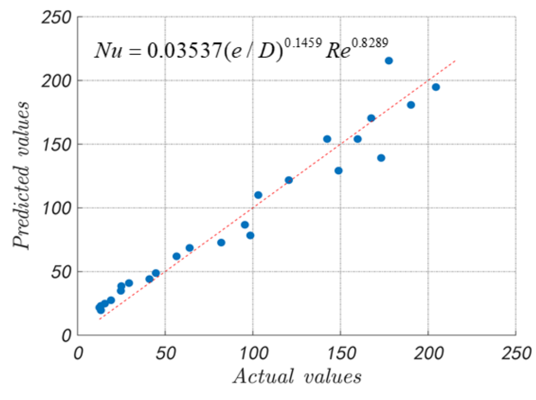

Figure 22. Predicted values vs. actual values for Nusselt number.

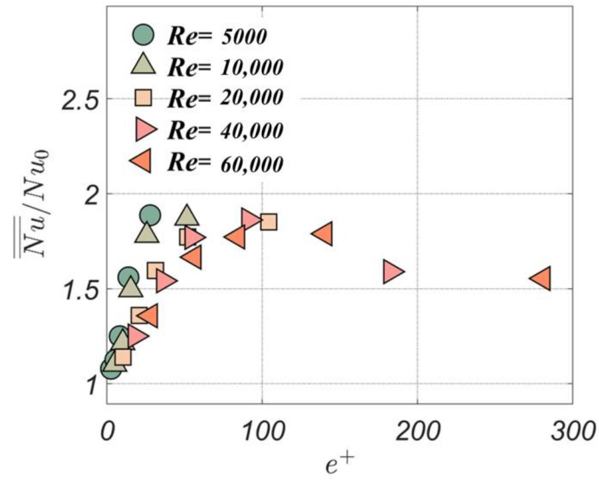

Figure 23. Nusselt number variation with e^+, for different Re.

In this study, a new non-dimensional scale $e^+/\sqrt{Re}$ is taken as the basis, and the results are shown in Figure 24. Within this non-dimensional scale, the heat transfer performance of micro ribs can be divided into three intervals. In the range of $0 < e^+/\sqrt{Re} < 10$, the heat transfer ability hardly increases with the increase in the non-dimensional scale. In the interval of $10 < e^+/\sqrt{Re} < 40$, the heat transfer ability increases with the increase in the non-dimensional scale. However, after $e^+/Re > 40$, the heat transfer ability between micro ribs decreases with the increase in the non-dimensional number.

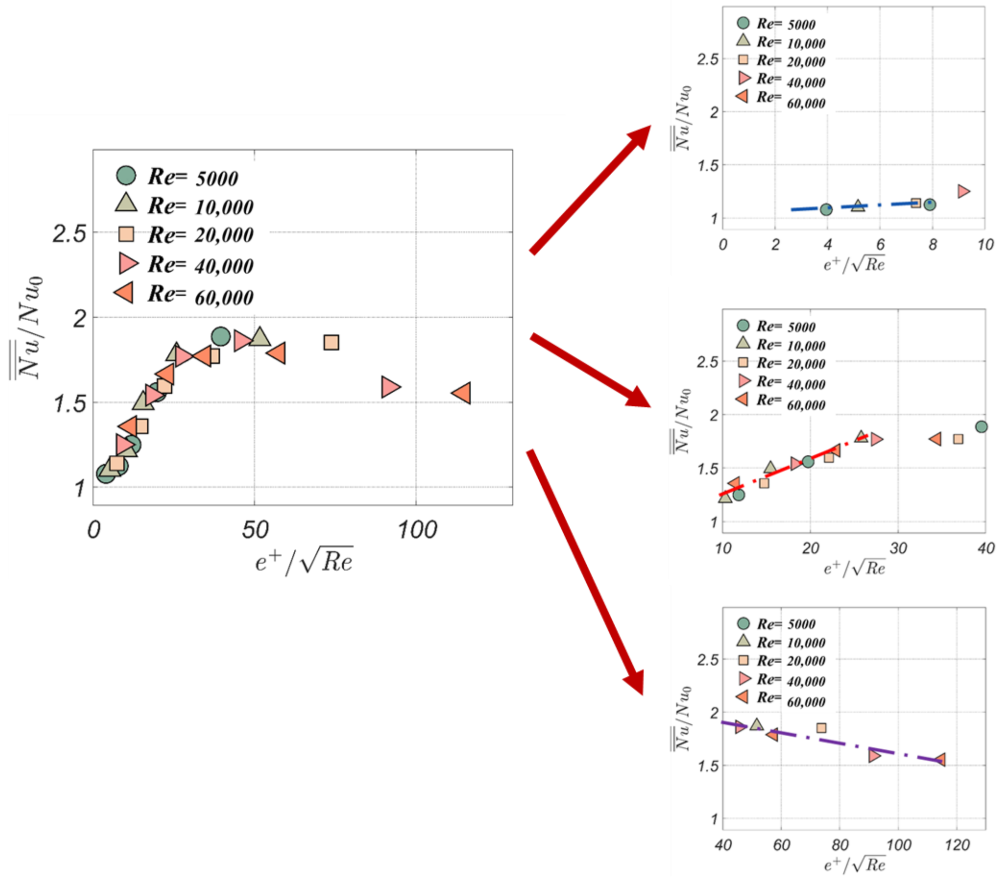

Figure 24. The non-dimensional number as a parameter of micro ribs for heat transfer.

It can be observed that the new non-dimensional number, as a better parameter to measure the heat transfer performance of micro ribs, differentiates the heat transfer performance of micro ribs at different Reynolds numbers and rib heights and reveals the optimal comprehensive performance range of micro ribs.

4.4. Effect of Micro Ribs on Overall Evaluation

By using the overall thermal performance (OTP) as an indicator to analyze the overall effectiveness of micro ribs, Figure 25 presents the results for different operating conditions. For low Reynolds numbers, the comprehensive performance of micro ribs continues to improve as the rib height increases. However, for higher Reynolds numbers, the comprehensive performance initially increases and then decreases with increasing rib height, indicating the existence of an optimal height. The analysis above indicates that as the rib height increases, although the resistance characteristics improve, the heat transfer performance no longer improves further. The right graph illustrates the results of a non-dimensional number based on the incoming boundary layer, which captures the trend of OTP well and indicates an optimal range of variation (30–60). It should be noted that this parameter's description of heat transfer enhancement tendencies is not as accurate as its description of OTP trends, primarily due to fluctuations in the resistance characteristics of micro ribs at low Reynolds numbers.

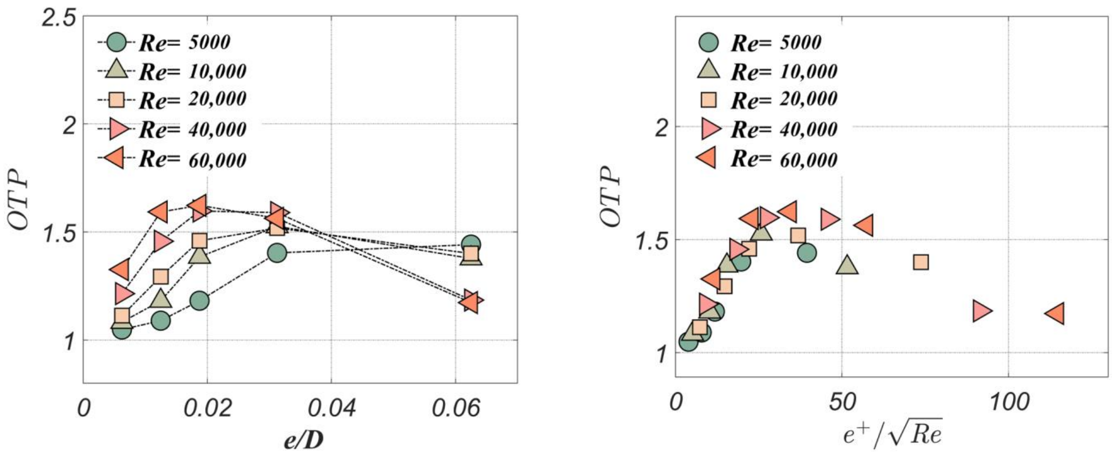

Figure 25. Overall evaluation of flow and heat transfer performance for e/D and $e^+/\sqrt{Re}$.

Finally, the heat transfer enhancement characteristic was evaluated from the perspective of OTP and compared with other classical data of 90° ribs originating from Han [2], Taslim [6], and Cho et al. [9], as shown in Figure 26.

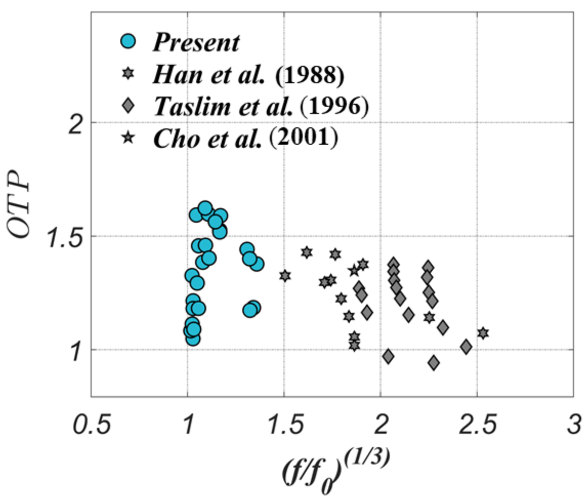

Figure 26. Overall evaluation of micro ribs compared with previous studies. From Han et al. [2], Taslim et al. [6], and Cho et al. [9].

Compared to previous studies, the overall performance (OTP) of micro ribs in this research revealed a higher cooling effectiveness. Within a specific parameter interval, the micro ribs improve the heat transfer performance by about 30% compared with the traditional 90° ribs. This optimized performance indicates the potential for achieving higher heat transfer efficiency and energy utilization in various practical applications through the design and application of micro ribs.

5. Conclusions

The present paper investigates the aerothermal dynamic performance in an array of micro-rib channels using both experimental and numerical methods. A PID-controlled segmented lumped parameter method was adopted to measure the heat transfer characteristics of rib channels. Numerical simulation was used to obtain flow and heat transfer information. The main conclusions from the present study are as follows:

(1) Regarding the drag characteristics of micro ribs, it was found that the drag continuously increases with the increase in rib height and is not sensitive to changes in Reynolds number, with only slight differences observed at low Reynolds numbers (Re = 5000–10,000). The formation of recirculation vortices between the ribs due to the increase in rib height is the main factor contributing to the increase in drag. These findings apply specifically to micro ribs with smaller heights.

(2) The heat transfer characteristics of micro ribs are greatly influenced by rib height and Reynolds number. At low Reynolds numbers, the heat transfer performance of micro ribs increases continuously with the increase in rib height. As the Reynolds number continues to increase, the heat transfer characteristics of micro ribs initially increase and then decrease with the increase in rib height. Analysis of the turbulent enhancement of the downstream flow caused by micro ribs under different operating conditions reveals that micro ribs are the main cause of heat transfer enhancement between ribs through the turbulent enhancement in the near-wall region of the boundary layer (y^+ = 20–55). With further increase in rib height, the region of turbulent enhancement is elevated, which leads to no further increase in heat transfer.

(3) An empirical correlation of heat transfer and resistance based on the experimental range in this study is proposed. The form of the correlation can further verify the aforementioned heat transfer resistance characteristics. Additionally, a dimensionless parameter $e^+/\sqrt{Re}$ related to the incoming boundary layer scale is proposed in this paper. This parameter can effectively reflect the heat transfer characteristics of micro ribs. It is revealed that micro ribs exhibit good overall heat transfer performance when this dimensionless parameter is between 20 and 55.

(4) Overall, the micro ribs investigated in this study demonstrate excellent heat transfer performance under specific operating conditions. This optimized performance indicates the potential for achieving higher heat transfer efficiency and energy utilization in various practical applications through the design and application of micro ribs.

Author Contributions: Conceptualization, K.Z. and X.L.; Methodology, K.Z. and X.L.; Software, K.Z.; Validation, K.Z.; Formal analysis, K.Z.; Investigation, K.Z.; Resources, K.Z.; Data curation, K.Z.; Writing—original draft, K.Z. and X.L.; Writing—review & editing, K.Z., X.L. and J.R.; visualization, K.Z.; Supervision, J.R.; Project administration, X.L. and J.R.; Funding acquisition, X.L. and J.R. All authors have read and agreed to the published version of the manuscript.

Funding: This research was funded by the National Science and Technology Major Project (J2019-III-0007-0050) and Tsinghua University Initiative Scientific Research Program.

Data Availability Statement: Not applicable.

Conflicts of Interest: The authors declare no conflict of interest.

Nomenclature

Bi	Biot number	[-]
D	Hydraulic diameter	[m]
f	Friction factor	[-]
H	Channel height	[m]
e	Rib height	
e^+	Rib dimensionless height	[-]
I	Turbulent intensity	[-]
K	Turbulent kinetic energy	[m^2/s^2]
Nu	Nusselt number	[-]
p	Rib pitch	[m]
Pr	Prandtl number	
q	Heat flux density	[W/m^2]
R	Resistance	[Ω]
Re	Reynolds number	[-]
S	Surface area	[m^2]
T	Temperature	[K]
T_f	Flow temperature	[K]
T_w	Wall temperature	[K]
U	Voltage	[V]
u_m	Bulk velocity	[m/s]
u, v, w	Velocity component in streamwise, wall-normal and spanwise direction	[m/s]
V	Velocity magnitude	[m/s]
X, Y, Z	Streamwise, wall normal and spanwise direction	[mm]
α	Thermal diffusivity	[-]
ΔP	Pressure loss	[Pa]
Λ	Thermal conductivity	[W/(m·k)]
ν	Kinematic viscosity	[m^2/s]
ρ	Density	[kg/m^3]

References

1. Webb, R.L.; Eckert, E.R.G.; Goldstein, R.J. Heat Transfer and Friction in Tubes with Repeated-Rib Roughness. *Int. J. Heat Mass Transf.* **1971**, *14*, 601–617. [CrossRef]
2. Han, J.C. Heat Transfer and Friction in Channels with Two Opposite Rib-Roughened Walls. *Trans. ASME J. Heat Transf.* **1984**, *106*, 744–781. [CrossRef]
3. Han, J. Heat-Transfer and Friction Characteristics in Rectangular Channels with Rib Turbulators. *J. Heat Transf.-Trans. ASME* **1988**, *110*, 321–328. [CrossRef]
4. Tanda, G. Heat Transfer in Rectangular Channels with Transverse and V-Shaped Broken Ribs. *Int. J. Heat Mass Transf.* **2004**, *47*, 229–243. [CrossRef]
5. Liou, T.; Hwang, J. Developing Heat-Transfer and Friction in a Ribbed Rectangular Duct with Flow Separation at Inlet. *J. Heat Transf.-Trans. ASME* **1992**, *114*, 565–573. [CrossRef]
6. Taslim, M.E.; Li, T.; Kercher, D.M. Experimental Heat Transfer and Friction in Channels Roughened with Angled, V-Shaped, and Discrete Ribs on Two Opposite Walls. *J. Turbomach.-Trans. ASME* **1996**, *118*, 20–28. [CrossRef]
7. Park, J.S.; Han, J.C.; Huang, Y.; Ou, S.; Boyle, R.J. Heat Transfer Performance Comparisons of Five Different Rectangular Channels with Parallel Angled Ribs. *Int. J. Heat Mass Transf.* **1992**, *35*, 2891–2903. [CrossRef]
8. SriHarsha, V.; Prabhu, S.V.; Vedula, R.P. Influence of Rib Height on the Local Heat Transfer Distribution and Pressure Drop in a Square Channel with 90 Degrees Continuous and 60 Degrees V-Broken Ribs. *Appl. Therm. Eng.* **2009**, *29*, 2444–2459. [CrossRef]
9. Cho, H.H.; Lee, S.Y.; Wu, S.J. The Combined Effects of Rib Arrangements and Discrete Ribs on Local Heat/Mass Transfer in a Square Duct. In *ASME Turbo Expo: Power for Land, Sea, & Air*; American Society of Mechanical Engineers: New York, NY, USA, 2001.
10. Tanda, G. Effect of Rib Spacing on Heat Transfer and Friction in a Rectangular Channel with 45 Degrees Angled Rib Turbulators on One/Two Walls. *Int. J. Heat Mass Transf.* **2011**, *54*, 1081–1090. [CrossRef]
11. Wright, L.M.; Gohardani, A.S. Effect of Turbulator Width and Spacing on the Thermal Performance of Angled Ribs in a Rectangular Channel (AR = 3:1). In *Volume 10: Heat Transfer, Fluid Flows, and Thermal Systems, Parts A, B, and C*; ASMEDC: Boston, MA, USA, 2008; pp. 1103–1113.
12. Hossain, J.; Curbelo, A.; Garrett, C.; Wang, W.; Kapat, J.; Thorpe, S.; Maurer, M. Use of Rib Turbulators to Enhance Postimpingement Heat Transfer for Curved Surface. *J. Eng. Gas Turbines Power* **2017**, *139*, 071901. [CrossRef]

13. Dees, J.E.; Bogard, D.G.; Ledezma, G.A.; Laskowski, G.M.; Tolpadi, A.K. Experimental Measurements and Computational Predictions for an Internally Cooled Simulated Turbine Vane with 90 Degree Rib Turbulators. *J. Turbomach.-Trans. ASME* **2012**, *134*, 061005. [CrossRef]
14. Coletti, F.; Scialanga, M.; Arts, T. Experimental Investigation of Conjugate Heat Transfer in a Rib-Roughened Trailing Edge Channel With Crossing Jets. *J. Turbomach.-Trans. ASME* **2012**, *134*, 041016. [CrossRef]
15. Liou, T.-M.; Chang, S.-W.; Chan, S.-P.; Liu, Y.-S. Particle Image Velocimetry Measurements in a Two-Pass 90 Degree Ribbed-Wall Parallelogram Channel. *J. Turbomach.-Trans. ASME* **2015**, *137*, 041012. [CrossRef]
16. Kaewchoothong, N.; Sukato, T.; Narato, P.; Nuntadusit, C. Flow and Heat Transfer Characteristics on Thermal Performance inside the Parallel Flow Channel with Alternative Ribs Based on Photovoltaic/Thermal (PV/T) System. *Appl. Therm. Eng.* **2021**, *185*, 116237. [CrossRef]
17. Bunker, R.S. Gas Turbine Cooling: Moving From Macro to Micro Cooling. In *Volume 3C: Heat Transfer*; American Society of Mechanical Engineers: San Antonio, TX, USA, 2013; p. V03CT14A002.
18. Nikuradse, J. Laws of Flow in Rough Pipes. 1950. Available online: https://www.researchgate.net/publication/285185167_Laws_of_flow_in_rough_pipes (accessed on 23 July 2023).
19. Jimenez, J. Turbulent flows over rough walls. *Annu. Rev. Fluid Mech.* **2004**, *36*, 173–196. [CrossRef]
20. Chung, D.; Hutchins, N.; Schultz, M.P.; Flack, K.A. Predicting the Drag of Rough Surfaces. In *Annual Review of Fluid Mechanics*; Moin, P., Stone, H.A., Eds.; Annual Reviews: Palo Alto, CA, USA, 2021; Volume 53, pp. 439–471. ISBN 978-0-8243-0753-0.
21. Wendt, B.J.; Greber, I.; Hingst, W.R. Structure and Development of Streamwise Vortex Arrays Embedded in a Turbulent Boundary Layer. *AIAA J.* **1993**, *31*, 319–325. [CrossRef]
22. Eibeck, P.A.; Eaton, J.K. Heat Transfer Effects of a Longitudinal Vortex Embedded in a Turbulent Boundary Layer. *J. Heat Transfer.* **1987**, *109*, 16–24. [CrossRef]
23. Pauley, W.R.; Eaton, J.K. The Effect of Embedded Longitudinal Vortex Arrays on Turbulent Boundary Layer Heat Transfer. *J. Heat Transfer.* **1994**, *116*, 871–879. [CrossRef]
24. Domaschke, N.; von Wolfersdorf, J.; Semmler, K. Heat Transfer and Pressure Drop Measurements in a Rib Roughened Leading Edge Cooling Channel. *J. Turbomach.* **2012**, *134*, 061006. [CrossRef]
25. Singh, S.K.; Raushan, P.K.; Debnath, K.; Mazumder, B.S. Effect of Surface Wave on Development of Turbulent Boundary Layer Over a Train of Rib Roughness. *J. Offshore Mech. Arct. Eng. Trans. ASME* **2019**, *141*, 061101. [CrossRef]
26. Davidson, L. Effect of Inclined Vortex Generators on Heat Transfer Enhancement in a Three-Dimensional Channel. *Numer. Heat Transf. Part A Appl.* **2001**, *39*, 433–448. [CrossRef]
27. Ravigururajan, T.S. A Comparative Study of Thermal Design Correlations for Turbulent Flow in Helical-Enhanced Tubes. *Heat Transf. Eng.* **1999**, *20*, 54–70. [CrossRef]
28. Mulhearn, P.J.; Finnigan, J.J. Turbulent Flow over a Very Rough, Random Surface. *Bound.-Layer Meteorol.* **1978**, *15*, 109–132. [CrossRef]
29. Savage, D.W. The Effect of Surface Roughness on Heat and Momentum Transfer. Ph.D. Thesis, Purdue University, West Lafayette, IN, USA, 1961; pp. 1–315.
30. Gabour, L.; Lienhard, J. Wall roughness effects on stagnation-point heat-transfer beneath an impinging liquid Jet. *J. Heat Transf.-Trans. ASME* **1994**, *116*, 81–87. [CrossRef]
31. Ren, Z.; Buzzard, W.C.; Ligrani, P.M.; Nakamata, C.; Ueguchi, S. Impingement Jet Array Heat Transfer: Target Surface Roughness Shape, Reynolds Number Effects. *J. Thermophys. Heat Transf.* **2017**, *31*, 346–357. [CrossRef]
32. Oda, Y.; Takeishi, K.; Motoda, Y.; Sugimoto, S.; Miyake, Y. Heat Transfer Characteristics of Pin-Fin Arrays with Ribs to Cool Combustor Liners. *J. Therm. Sci. Technol.* **2009**, *4*, 507–517. [CrossRef]
33. Hahn, T.; Deakins, B.; Buechler, A.; Kumar, S.; Amano, R.S. Experimental Analysis of the Heat Transfer Variations within an Internal Passage of a Typical Gas Turbine Blade Using Varied Internal Geometries. In *Volume 5: 6th International Conference on Micro- and Nanosystems; 17th Design for Manufacturing and the Life Cycle Conference*; American Society of Mechanical Engineers: Chicago, IL, USA, 2012; pp. 851–858.
34. Benson, M.J.; Bindon, D.; Cooper, M.; Davidson, F.T.; Duhaime, B.; Helmer, D.; Woodings, R.; Van Poppel, B.P.; Elkins, C.J.; Clark, J.P. Detailed Velocity and Heat Transfer Measurements in an Advanced Gas Turbine Vane Insert Using Magnetic Resonance Velocimetry and Infrared Thermometry. *J. Turbomach.-Trans. ASME* **2022**, *144*, 021009. [CrossRef]
35. Choi, J.; Mhetras, S.; Han, J.-C.; Lau, S.C.; Rudolph, R. Film Cooling and Heat Transfer on Two Cutback Trailing Edge Models With Internal Perforated Blockages. *J. Heat Transf.* **2008**, *130*, 012201. [CrossRef]
36. Cunha, F.J.; Chyu, M.K. Trailing-Edge Cooling for Gas Turbines. *J. Propuls. Power* **2006**, *22*, 286–300. [CrossRef]
37. Amro, M.; Weigand, B.; Poser, R.; Schnieder, M. An Experimental Investigation of the Heat Transfer in a Ribbed Triangular Cooling Channel. *Int. J. Therm. Sci.* **2007**, *46*, 491–500. [CrossRef]
38. Funazaki, K.; Odagiri, H.; Horiuchi, T.; Kazari, M. Detailed Studies on the Flow Field and Heat Transfer Characteristics Inside a Realistic Serpentine Cooling Channel with a S-Shaped Inlet. In *ASME Turbo Expo: Turbomachinery Technical Conference and Exposition*; AMER Soc Mechanical Engineers: New York, NY, USA, 2018; Volume 5b, p. V05BT13A010.
39. Schüler, M.; Zehnder, F.; Weigand, B.; von Wolfersdorf, J.; Neumann, S.O. The Effect of Side Wall Mass Extraction on Pressure Loss and Heat Transfer of a Ribbed Rectangular Two-Pass Internal Cooling Channel. *J. Turbomach.* **2010**, *133*, 021002. [CrossRef]

40. Saha, K.; Acharya, S. *Heat Transfer Enhancement Using Angled Grooves as Turbulence Promoters*; American Society of Mechanical Engineers Digital Collection: New York, NY, USA, 2013.
41. Tariq, A.; Sharma, N.; Mishra, M. Aerothermal Characteristics of Solid and Slitted Pentagonal Rib Turbulators. *J. Heat Transf.-Trans. ASME* **2018**, *140*, 061901. [CrossRef]
42. Moffat, R.J. Describing the Uncertainties in Experimental Results. *Exp. Therm. Fluid Sci.* **1988**, *1*, 3–17. [CrossRef]
43. Fan, J.F.; Ding, W.K.; Zhang, J.F.; He, Y.L.; Tao, W.Q. A Performance Evaluation Plot of Enhanced Heat Transfer Techniques Oriented for Energy-Saving. *Int. J. Heat Mass Transf.* **2009**, *52*, 33–44. [CrossRef]